

# Understanding Dimethyl Methylphosphonate Adsorption and Decomposition on Mesoporous CeO<sub>2</sub>

Tianyu Li, Roman Tsyshevsky, Lucas Algrim, Monica McEntee, Erin M. Durke, Bryan Eichhorn, Christopher Karwacki, Michael R. Zachariah, Maija M. Kuklja,\* and Efrain E. Rodriguez\*



Cite This: *ACS Appl. Mater. Interfaces* 2021, 13, 54597–54609



Read Online

ACCESS |



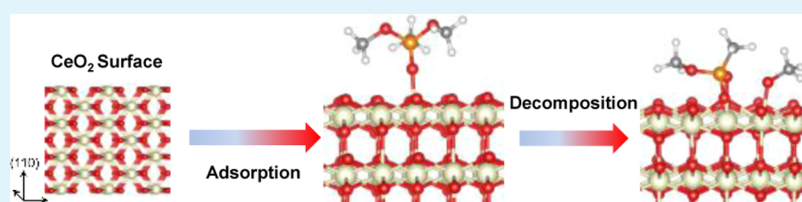
Metrics & More



Article Recommendations



Supporting Information



**ABSTRACT:** The increased risk of chemical warfare agent usage around the world has intensified the search for high-surface-area materials that can strongly adsorb and actively decompose chemical warfare agents. Dimethyl methylphosphonate (DMMP) is a widely used simulant molecule in laboratory studies for the investigation of the adsorption and decomposition behavior of sarin (GB) gas. In this paper, we explore how DMMP interacts with the as-synthesized mesoporous CeO<sub>2</sub>. Our mass spectroscopy and *in situ* diffuse reflectance infrared Fourier transform spectroscopy measurements indicate that DMMP can dissociate on mesoporous CeO<sub>2</sub> at room temperature. Two DMMP dissociation pathways are observed. Based on our characterization of the as-synthesized material, we built the pristine and hydroxylated (110) and (111) CeO<sub>2</sub> surfaces and simulated the DMMP interaction on these surfaces with density functional theory modeling. Our calculations reveal an extremely low activation energy barrier for DMMP dissociation on the (111) pristine CeO<sub>2</sub> surface, which very likely leads to the high activity of mesoporous CeO<sub>2</sub> for DMMP decomposition at room temperature. The two reaction pathways are possibly due to the DMMP dissociation on the pristine and hydroxylated CeO<sub>2</sub> surfaces. The significantly higher activation energy barrier for DMMP to decompose on the hydroxylated CeO<sub>2</sub> surface implies that such a reaction on the hydroxylated CeO<sub>2</sub> surface may occur at higher temperatures or proceed after the pristine CeO<sub>2</sub> surfaces are saturated.

**KEYWORDS:** chemical warfare agent, DMMP, mesoporous, cerium oxide, surface exposure, *in situ* DRIFTS, DFT modeling, decomposition reaction mechanisms

## 1. INTRODUCTION

The development of materials for protection against the chemical warfare agent (CWA) exposure has increased in need, not only for military personnel but for civilians as well. However, an understanding of the fundamental interactions between CWAs and protective materials is lacking. Recent efforts have been made to develop multiple characterization techniques to study the fundamental interactions between CWAs and potential candidate materials.<sup>1</sup> Some of the most notorious CWAs are the G-series nerve agents, specifically sarin (GB) and soman (GD), shown in Scheme 1a,b. Conventional means of protection against CWAs are through gas molecule adsorption and decomposition. Candidate materials for protection should possess large surface areas that are highly reactive toward CWAs. CWA molecules should bind strongly and decompose on the surfaces of these materials. Traditional and currently used protection or filtration materials are mostly porous carbon-based materials. Though porous carbon-based materials possess considerable surface areas, their protection against CWAs relies on

reversible physical adsorption.<sup>2</sup> The interaction between toxic molecules and the surface of carbon-based filter materials is relatively weak. Molecules can be easily desorbed at low vapor pressure, which can lead to secondary damage. Impregnation of carbon-based materials with metal oxides can improve the capacity of filter materials to defeat CWAs. For example, ASZM-TEDA-activated carbon impregnated with copper, silver, zinc, molybdenum, and triethylenediamine is used as a filter material in gas masks.<sup>3</sup> Metal oxides are also considered as potential filter materials for protection against CWAs<sup>4–7</sup> because of their versatile surface chemistry toward different molecules. However, the relatively low surface area of metal

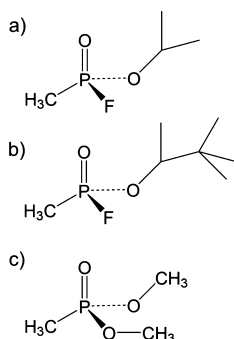
Received: August 30, 2021

Accepted: October 21, 2021

Published: November 3, 2021



**Scheme 1. Molecular Structures of (a) Nerve Agent Sarin, (b) Nerve Agent Soman, and (c) Their Simulant Molecule DMMP**



oxides in comparison with that of carbon-based materials implied that so far, there have been certain limitations on using them as filter materials. Recent studies show that the surface area of metal oxides can be considerably increased by fabricating mesoporous metal oxides.<sup>8,9</sup> Results of these studies potentially pave the way for the application of metal oxides as effective filter materials for protection against CWAs. Dimethyl methylphosphonate (DMMP, Scheme 1c) is widely used as a relatively benign simulant molecule of GB due to the structural similarity and similar vapor pressure. Generally, materials reactive toward DMMP decomposition are also very reactive toward sarin, such as  $\text{TiO}_2$ <sup>10–13</sup> and  $\text{Zr}(\text{OH})_4$ ,<sup>14,15</sup> despite certain differences in the reaction mechanisms.

DMMP interaction on different binary metal oxides, such as  $\text{Al}_2\text{O}_3$ ,<sup>16</sup>  $\text{TiO}_2$ ,<sup>10–12</sup>  $\text{CuO}$ ,<sup>17,18</sup>  $\text{MoO}_3$ ,<sup>19,20</sup>  $\text{Fe}_2\text{O}_3$ ,<sup>21</sup>  $\text{ZnO}$ ,<sup>22</sup>  $\text{ZrO}_2$ ,<sup>23</sup> and  $\text{CeO}_2$ ,<sup>24</sup> has been studied experimentally and theoretically. DMMP reactivity on  $\text{TiO}_2$ ,  $\text{CuO}$ ,  $\text{Y}_2\text{O}_3$ , and  $\text{CeO}_2$  has been reported, with DMMP dissociation observed at room temperature. Fluorite  $\text{CeO}_2$  draws extensive attention in many fields of catalysis and surface reactions such as photocatalytic dye degradation, electrocatalytic water splitting/ $\text{CO}$  reduction, fuel/ $\text{CO}$  conversion, and oxidation.<sup>25–27</sup>  $\text{CeO}_2$  demonstrates high reactivity in many catalytic and noncatalytic reactions due to its unique surface structure and the high reactivity of  $\text{Ce}^{4+}$ . Several studies on the decontamination of phosphorus containing compounds with  $\text{CeO}_2$  demonstrate ceria's high activity toward dephosphorylation.<sup>24,28–31</sup> DMMP dissociation is no exception. Chen et al.<sup>24</sup> studied the interaction of DMMP on the  $\text{CeO}_2$  (111) single crystal surface. They concluded based on the observed DMMP dissociation that  $\text{CeO}_2$  can be used as a potential filter material for protection against CWAs.<sup>24</sup> However, results obtained from single crystal surface experiments are far from practical applications due to the low surface area of samples and experimental conditions that are significantly different from atmospheric conditions. Additionally, a fundamental understanding of why  $\text{CeO}_2$  is reactive toward DMMP and how DMMP dissociates on the  $\text{CeO}_2$  is still lacking.

In this paper, we report the results of the most comprehensive (thus far) joint experimental and theoretical study of DMMP adsorption and decomposition on mesoporous  $\text{CeO}_2$ . To study the interaction of DMMP with  $\text{CeO}_2$ , we synthesized mesoporous  $\text{CeO}_2$  with a reported nanocasting method.<sup>32,33</sup> The as-synthesized mesoporous  $\text{CeO}_2$  has a relatively large surface area, making it practical for application as an adsorber. Adsorption and decomposition of DMMP on mesoporous  $\text{CeO}_2$  were studied using mass spectroscopy and

*in situ* diffuse reflectance infrared Fourier transform spectroscopy (DRIFTS). Density functional theory (DFT) modeling of DMMP interactions with pristine and hydroxylated  $\text{CeO}_2$  (110) and (111) surfaces was conducted to interpret the experimental measurements. We observed the DMMP decomposition through both mass spectroscopy and DRIFTS measurements at room temperature. DFT modeling shows that although both pristine and hydroxylated  $\text{CeO}_2$  surfaces decompose DMMP, it is the pristine surfaces that are more reactive than the hydroxylated ones. Our combined experimental and theoretical studies provide fundamental insights into the key parameters for designing  $\text{CeO}_2$ -based materials to defeat chemical agents similar to DMMP, such as GB.

## 2. EXPERIMENTAL SECTION

**2.1. Synthesis of Templated Mesoporous  $\text{CeO}_2$ .** Mesoporous  $\text{CeO}_2$  was synthesized via a nanocasting method similar to the previously reported approach.<sup>32,33</sup> The silica template KIT-6 was first prepared via a reported method,<sup>34</sup> for which 85 °C was used as the aging temperature during the KIT-6 synthesis. In our typical synthesis of mesoporous  $\text{CeO}_2$ , 0.5000 g of as-prepared KIT-6 silica was initially dispersed in 20.0 mL of 95% ethanol. Then, 1.362 g of  $\text{Ce}(\text{NO}_3)_3 \cdot 6\text{H}_2\text{O}$  was also dissolved in the same solution. The mixture was stirred at room temperature until all solvents were evaporated and the mixture became a dry powder. The powder was later transferred to a glass vial (a diameter of ~5 mm) and calcined at 560 °C for 6 h (a ramping rate of 1 °C/min). During the calcination step,  $\text{Ce}(\text{NO}_3)_3 \cdot 6\text{H}_2\text{O}$  decomposes and oxidizes to pure  $\text{CeO}_2$ . To fully remove the silica template, the  $\text{CeO}_2$ /KIT-6 composite was soaked in 2 M NaOH solution at 80 °C overnight; this step was repeated three times. After washing three times with distilled water and twice with ethanol, the final mesoporous  $\text{CeO}_2$  product was dried in air at 80 °C overnight and then at 150 °C for an additional 24 h.

**2.2. Surface and Structural Characterization of Mesoporous  $\text{CeO}_2$ .** The transmission electron microscopy (TEM) image was taken using a JEOL JEM 2100 LaB6 TEM system. The powder X-ray diffraction (XRD) pattern was recorded on the Bruker D8 Advance diffractometer, with  $\text{Cu K}\alpha/\text{K}\beta$  radiation. Rietveld refinements were performed using a TOPAS 5.<sup>35</sup> X-ray small-angle scattering (SAXS) patterns were collected using a Xenocs Xeus SAXS/WAXS/GISAXS system. The nitrogen adsorption isotherms were measured using a Micromeritics ASAP 2020 porosimeter test station, and the surface area was calculated by applying the Brunauer–Emmett–Teller (BET) equation on the adsorption data obtained at  $P/P_0$  between 0.05 and 0.35. The pore size distributions were calculated by analyzing the adsorption branch of the  $\text{N}_2$  sorption isotherm using the Barret–Joyner–Halenda method. Raman spectroscopy was carried out with a Yvon Jobin LabRam ARAMIS using a 532 nm laser source. Ce 3d and O 1s spectra were collected on a Kratos Axis 165 X-ray photoelectron spectrometer operating in the hybrid mode using Al  $\text{K}\alpha$  monochromatic X-rays at 280 W. All X-ray photoelectron spectrometry (XPS) spectra were calibrated to the C 1s peak at 284.80 eV, and fits were performed using CasaXPS. Shirley background was used for background subtraction, and the peaks were fit with a 30% Gaussian + 70% Lorentzian peak shape profile.

**2.3. CO Adsorption IR Spectroscopy on  $\text{CeO}_2$ .** CO adsorption studies on  $\text{CeO}_2$  were performed in a high-vacuum chamber with a base pressure of  $3 \times 10^{-9}$  Torr. A more detailed description of the vacuum chamber is provided elsewhere.<sup>36</sup>  $\text{CeO}_2$  was pressed into a 0.004" thick W-grid and attached to the sample mount via stainless-steel clamps connected to copper rods. The copper rods were attached to a power supply, allowing for resistive heating of the sample up to ~1000 K at a resolution of  $\pm 0.1$  K. Before introducing CO into the vacuum chamber, the sample was heated up to 450 K for 30 min in order to remove  $\text{H}_2\text{O}$  and hydrocarbon impurities. After heating, the surface was cooled down with  $\text{LN}_2$  (~140 K), and an IR spectrum was obtained for the  $\text{CeO}_2$  sample. An IR spectrum was taken for the W-grid without any  $\text{CeO}_2$  powder and used as the

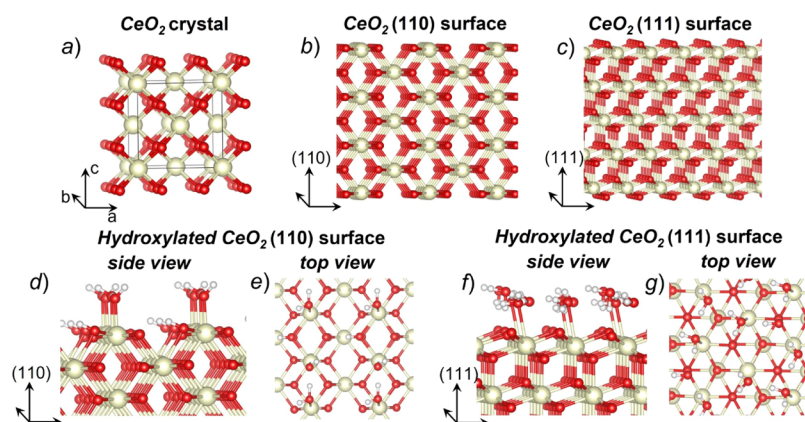


**Figure 1.** (a) Structure of the  $\text{CeO}_2$  crystal; structures of  $\text{CeO}_2$  (b) (110) and (c) (111) surfaces; (d) side and (e) top views of the hydroxylated  $\text{CeO}_2$  (110) surface; and (f) side and (g) top views of the hydrated  $\text{CeO}_2$  (111) surface.

background. Each IR spectrum contains an average of 256 interferograms at a resolution of  $2\text{ cm}^{-1}$ .

Subsequently,  $10^{-2}$  Torr CO vapor was introduced into the vacuum chamber. An IR spectrum was taken and was subtracted from the IR spectrum of  $\text{CeO}_2$  prior to CO exposure. The subtracted spectrum represents a difference spectrum showing the CO adsorption on the  $\text{CeO}_2$  surface.

**2.4. Detection of DMMP Decomposition on Mesoporous  $\text{CeO}_2$  via Mass Spectrometry.** Mass spectrometry was used to detect any reaction products from the interaction of mesoporous  $\text{CeO}_2$  and DMMP. The measurements made with a mass spectrometer used an experimental setup described in the previous work<sup>2</sup> and again briefly described here. Before the analysis with the mass spectrometer, the  $\text{CeO}_2$  sample was heated to  $200\text{ }^\circ\text{C}$  to remove any potential surface contaminants. Three mass flow controllers regulated the flow of dry argon, argon saturated with water, and DMMP, all of which were combined to produce a 35 mL/min total flow that was  $0.4P/P_0$  DMMP and 4% relative humidity at room temperature. The combined flow was passed into a 4.7625 mm (3/16") ID quartz tube which holds the  $\text{CeO}_2$  sample, supported by inert glass wool. The quartz tube was heated at  $10\text{ }^\circ\text{C}/\text{min}$  to  $325\text{ }^\circ\text{C}$  and held for 3 h before cooling to room temperature, where it was kept for approximately 7 h before heating again. This temperature cycle was repeated multiple times. Downstream from the material, a capillary line sampled the gas mixture into the quadrupole mass spectrometer, which collected the full mass scans up to  $m/z$  125. All-time traces are normalized to  $m/z$  36 (an isotope of argon) to minimize the effects of the signal drift.

**2.5. In Situ DRIFTS of DMMP Adsorption/Decomposition on Mesoporous  $\text{CeO}_2$ .** For the DRIFTS measurements, a Harrick Scientific Praying Mantis DRA optical accessory was used with an associated Harrick Scientific high-temperature reaction chamber HVC-DRP-5 and a temperature controller unit (110 V, ATC-024-3). Prior to DMMP exposure, mesoporous  $\text{CeO}_2$  powder was heated under the 25 mL/min Ar flow at  $200\text{ }^\circ\text{C}$  for 2 h to remove as much physisorbed water as possible and then cooled to room temperature. We were mainly interested in the interaction between mesoporous  $\text{CeO}_2$  and strongly adsorbed DMMP molecules. Additionally, we wanted to minimize the DMMP contamination in our DRIFTS system. Thus, a swift injection approach was employed to introduce DMMP into the DRIFTS cell containing mesoporous  $\text{CeO}_2$  powder. In a typical experiment, mesoporous  $\text{CeO}_2$  powder in the cell was under a constant 25 mL/min Ar flow. Then, 2 mL of saturated DMMP vapor carried by  $\text{N}_2$  was quickly injected into the system using a delay-controlled electronic injector. The illustration of such a system is provided in the Supporting Information. The injections occurred every 20 min. Between the injections, DRIFTS spectra were collected every 30 s, allowing for the observation of the strong interaction between the substrate ( $\text{CeO}_2$ ) and the molecule of interest

(DMMP). In total, 10 DMMP injections were performed. The instrument setup is presented in the Supporting Information.

**2.6. DFT Modeling of DMMP Interacting with  $\text{CeO}_2$  Surfaces.** Solid-state periodic calculations were performed with the DFT<sup>37,38</sup> using the GGA PBE<sup>39</sup> functional and projector augmented-wave pseudo-potentials,<sup>40</sup> as implemented in the VASP code.<sup>41–43</sup> Hubbard's parameter  $U^{44}$  was introduced to account for Ce 4f orbitals and was set to 4.0 eV, in accordance with the reported literature.<sup>45</sup> Grimme's D2<sup>46</sup> corrections were added to account for weak van der Waals interactions. In simulating ideal bulk crystals, atomic coordinates and lattice constants were allowed to relax simultaneously without any symmetry constraints. The convergence criterion for electronic steps was set to  $10^{-5}$  eV, and the maximum force acting on any atom was set to not exceed  $0.01\text{ eV}/\text{\AA}$ . The kinetic energy cutoff was set to 520 eV. In modeling the  $\text{CeO}_2$  crystal, an  $8 \times 8 \times 8$  Monkhorst–Pack  $k$ -point mesh was used. The calculated lattice parameters of the  $\text{CeO}_2$  cubic unit cell (Figure 1a) with the  $Fm\bar{3}m$  space group,  $a = 5.37\text{ \AA}$ , agree with the experimental lattice vectors ( $a = 5.41\text{ \AA}$ ) within  $\sim 1\%$ .

Our calculations of DMMP adsorption and decomposition were limited to modeling reactions on the most stable surfaces, including (110) and (111) surfaces (Figure 1b,c), observed in our experiments. The model slab of the (110) surface contained 252 atoms with the supercell lattice vectors of  $a = 16.23\text{ \AA}$ ,  $b = 14.92\text{ \AA}$ , and  $c = 31.61\text{ \AA}$ . The model slab of the (111) surface contained 240 atoms with the supercell lattice vectors of  $a = b = 15.03\text{ \AA}$  and  $c = 34.37\text{ \AA}$ . A vacuum layer of 20  $\text{\AA}$  placed on the top of the  $\text{CeO}_2$  surfaces served to minimize the interactions between the supercells in the  $z$ -direction and to avoid any significant overlap between wave functions of periodically translated cells. All surface calculations were performed at the  $G$ -point only. Kinetic energy cutoffs in modeling  $\text{CeO}_2$  (110) and (111) surfaces were set to 520 eV. The convergence criterion for electronic steps was set to  $10^{-5}$  eV, and the maximum force acting on any atom was set to not exceed  $0.03\text{ eV}/\text{\AA}$ .

In modeling DMMP interactions with  $\text{CeO}_2$  surfaces in the presence of water, a monolayer of water was added on  $\text{CeO}_2$  (110) and (111) surfaces. Our calculations show that the monolayer of water containing intact and dissociated water (OH group) molecules is the most energetically favorable configuration for the  $\text{CeO}_2$  (110) surface (Figure 1d,e), whereas for the  $\text{CeO}_2$  (111) surface, the monolayer of water containing only intact water molecules corresponds to the most energetically favorable configuration (Figure 1f,g) (see the Supporting Information for more discussion).

Minimal energy paths in the VASP periodic calculations were obtained with the standard nudged elastic band method.<sup>47</sup> Atomic positions were relaxed using the conjugate gradient and quasi-Newtonian methods within a force tolerance of  $0.05\text{ \AA}/\text{eV}$ . The convergence criterion for electronic steps was set to  $10^{-5}$  eV.

### 3. RESULTS

**3.1. Bulk and Surface Properties of Mesoporous CeO<sub>2</sub>.** The characterization of the structure and surface of synthesized mesoporous CeO<sub>2</sub> is presented in Figure 2. The

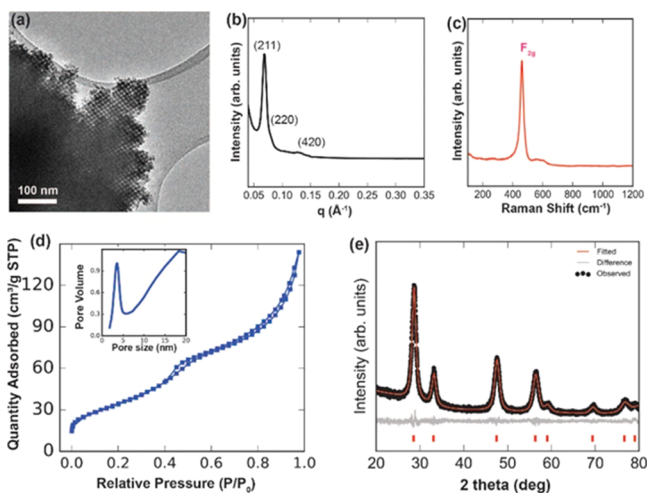


**Figure 2.** Structural and surface characterization of as-synthesized mesoporous CeO<sub>2</sub>: (a) TEM. (b) SAXS. (c) Raman Spectroscopy. (d) Nitrogen adsorption isotherm and pore size distribution (inset). (e) XRD pattern and Rietveld refinement fit.

resulting mesoporous morphology and structure resemble the results previously reported for mesoporous ceria.<sup>33,34</sup> An ordered mesoporous structural property is visible from the TEM image (Figure 2a). Diffraction peaks for the (211), (220), and (420) reflections of the structure are observed in the SAXS pattern (Figure 2b), which confirm the ordered porous structure of a body-centered cubic structure (space group *Ia3d*). Nitrogen adsorption isotherms and the corresponding pore size distribution curve (inset) are displayed in Figure 2d. The extracted BET surface area is 130.4 m<sup>2</sup>/g, and the mean pore size is approximately 3.6 nm. XRD patterns (Figure 2e) confirm the pure phase of cubic CeO<sub>2</sub> with the fluorite-type structure (space group *Fm3m*). We note that the diffraction peaks in the XRD pattern severely broaden due to the nanocrystalline nature of mesoporous CeO<sub>2</sub>. The Rietveld refinement indicates that the lattice parameter is 5.4138(8) Å and the average crystallite size is 11.8(1) nm. Raman spectroscopy (Figure 2c) shows a major F<sub>2g</sub> vibration mode, also indicative of phase-pure CeO<sub>2</sub> with the fluorite-type structure. Similar to that in the XRD patterns, the pronounced peak broadening in the Raman spectrum arises from the quantum size confinement of nanocrystalline CeO<sub>2</sub>.<sup>48</sup> The asymmetric peak shape is largely due to the surface states<sup>49</sup> because of the high surface area of mesoporous CeO<sub>2</sub>.

The Ce 3d XPS spectra are displayed in Figure 3a. The spectra are fit by employing previously reported parameters.<sup>50</sup> Applying only Ce<sup>4+</sup> components afford a good fit to the spectrum, which implies that Ce<sup>4+</sup> predominates as the Ce species on the surface. The O 1s XPS spectra (Figure 3b) suggests the presence of two major types of oxygen, namely, 40% lattice oxygen (O<sup>2-</sup>) at 529.3 eV and 60% surface oxygen (–OH) at 531.5 eV. The O 1s XPS spectra also indicate that a large fraction of the surface of mesoporous CeO<sub>2</sub> is hydroxylated (–OH-terminated), which is common for metal oxides under ambient conditions.

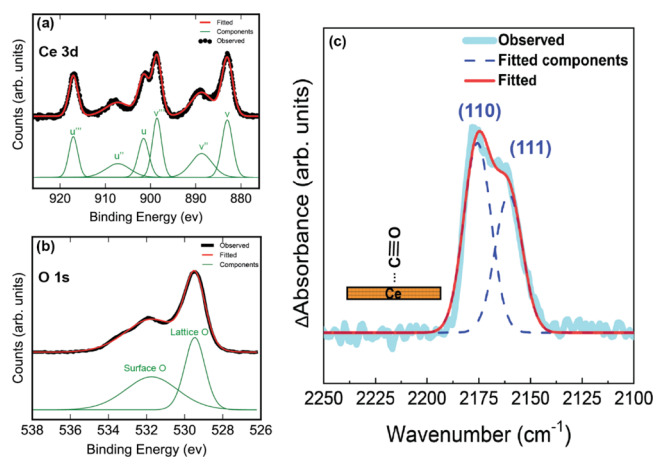


**Figure 3.** (a) Ce 3d XPS spectra and fitting of mesoporous CeO<sub>2</sub>. (b) O 1s XPS spectra and fitting of mesoporous CeO<sub>2</sub>. (c) IR spectra of CO stretching when CO is adsorbed onto mesoporous CeO<sub>2</sub>.

For a crystalline material, its chemical reactivity can vary greatly depending on which crystalline surfaces are exposed since surface properties (such as the polarity, surface energy, hydrophilicity, and coordination configuration of surface atoms) differ considerably from surface to surface. Thus, the determination of the exposed surfaces (facets) is crucial to understand the surface chemistry of certain materials. For a material with a single crystal surface (film), the exposed surface can be determined by surface diffraction methods or scanning tunneling microscopy (STM). High-resolution TEM is normally applied to visualize the exposed surface of nanocrystals. However, it is challenging to use the above-mentioned techniques for the determination of exposed surfaces in mesoporous materials. On one hand, the three-dimensional pore structure makes it impossible to obtain the information about the interior of pores with STM and TEM. On the other hand, TEM only gives very localized information instead of statistical information of the exposed surface if more than one surface is exposed. Therefore, we followed well-established studies whereby CO molecules adsorb on the different surfaces of CeO<sub>2</sub>; since the C–O stretching frequencies correlate to the coordination strength and degree of back-bonding between CO and Ce atoms on the surface, one can learn about the nature of the exposed ceria surface.<sup>51,52</sup> Infrared spectroscopy can detect the C–O stretching frequencies, and the large penetration depth of the IR beam (hundreds of nanometers to tens of microns) makes it ideal to gain information inside the pores of mesoporous materials.

Here, we applied an indirect method to gain the statistical information on exposed surfaces of mesoporous CeO<sub>2</sub>. As a probe molecule, CO is first dosed into mesoporous CeO<sub>2</sub>, followed by the detection of C–O stretching with transmission IR spectroscopy. The results are displayed in Figure 3c. Two major CO stretching frequencies are visible. The peak around 2178 cm<sup>-1</sup> corresponds to CO adsorbed on the (110) CeO<sub>2</sub> surface. The 2159 cm<sup>-1</sup> peak corresponds to CO adsorbed on the (111) CeO<sub>2</sub> surface.<sup>51,52</sup> A Gaussian peak profile is used to fit the peaks within the spectrum. The fitting implies that the (110) surface accounts for 56% of the exposed surface of the mesoporous CeO<sub>2</sub> system and the (111) surface the remaining 44% of the exposed surface. It is worth noting that CO adsorbs on the surface of CeO<sub>2</sub> through the coordination between CO and exposed Ce metal sites.<sup>52</sup> The observation of CO

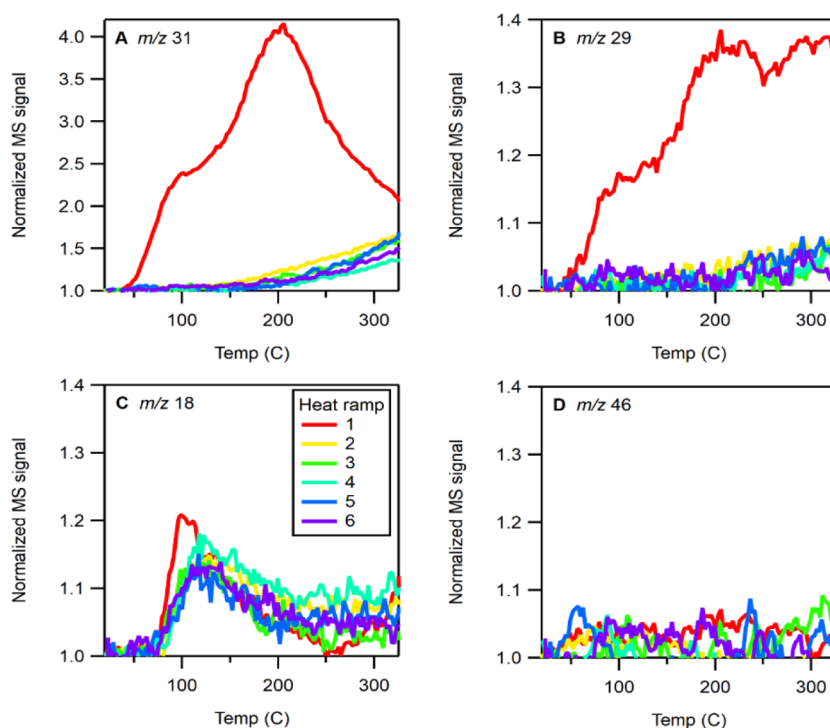


**Figure 4.** Mass spectrum signal originating from water and DMMP decomposition products as ceria is heated. The panels show traces of  $m/z$  31 (A) for the methanol product and  $m/z$  29 (B), which can be attributed to methanol or formaldehyde. Panel C shows  $m/z$  18, which is due to water, and panel D shows  $m/z$  46, which is due to the dimethyl ether product.

stretching modes in the IR spectrum indicates the considerable amounts of exposed (or undercoordinated) Ce atoms on the surface of mesoporous  $\text{CeO}_2$  despite the fact that our XPS results show that a large part of the surface is hydroxylated ( $-\text{OH}$ -terminated).

**3.2. DMMP Decomposition Product at Elevated Temperatures.** Time traces of common product ions from DMMP dosing onto mesoporous  $\text{CeO}_2$  are plotted in Figure 4. Each  $m/z$  trace is plotted against temperature and is colored according to the number of heat ramps. Across the entire measured temperature range in the first heat ramp, methanol is observed as a major product ( $m/z$  31 signal in Figure 4A), which is a common decomposition product of DMMP.<sup>22,53</sup> It is noticeable that the methanol signal is first observed near room temperature ( $\sim 40$  °C), implying the high reactivity of mesoporous  $\text{CeO}_2$  toward DMMP dissociation. In the methanol production trace plot (Figure 4A), a bimodal peak is observed at 200 °C and a small shoulder appears at 100 °C, implying that there are possibly two reaction pathways for DMMP decomposition on mesoporous  $\text{CeO}_2$  to produce methanol.

The two different peak temperatures of methanol production suggest that the two pathways of DMMP decomposition have different activation barriers. The mass spectra alone are insufficient to determine whether the methanol observed near 100 °C is generated at that point or whether it readily forms through decompositions at room temperature, followed by desorption at higher temperatures. In the subsequent heat ramps, a dramatic decrease in the methanol production was noted, and the methanol signal curve is very different from the first ramp (i.e., peaks disappear). Such phenomena reveal that the DMMP decomposition on  $\text{CeO}_2$  is a surface reaction instead of a heterocatalytic reaction. After the first cycle of DMMP

interacting with mesoporous  $\text{CeO}_2$ , the surface of  $\text{CeO}_2$  is changed and is shown to be deactivated toward DMMP decomposition. The changing of the  $\text{CeO}_2$  surface after the first ramp can also be confirmed by looking at the water trace. Moisture is always present in the system. As shown in Figure 4C, we observed a water signal peak after 100 °C for every heating ramp, which we attribute to the thermal desorption of the water molecules on the  $\text{CeO}_2$  surface. However, the water desorption peak appears at 100 °C in the first heat ramp, but in all successive ramps, the temperature slightly elevates to 125 °C, confirming a change in the surface after the first ramp of the DMMP reaction.

Figure 4B shows the time traces for  $m/z$  29, which can be attributed to methanol or formaldehyde. It can be seen that the  $m/z$  29 trace mostly mimics that of  $m/z$  31 due to the majority of the  $m/z$  29 signal originating from MeOH. However, one difference is observed in heat ramp 1 above 250 °C. Because  $m/z$  29, and not  $m/z$  31, rises to form a third mode at high temperature ( $>250$  °C), this third mode can be reasonably assigned to formaldehyde, which has been observed as a DMMP decomposition product from  $\text{CeO}_2$ .<sup>24</sup> The trace of  $m/z$  46 (Figure 4D) is the molecular ion of dimethyl ether, another common DMMP decomposition product that has been obtained from  $\text{CeO}_2$  in the air as well as from other metal oxides<sup>54</sup> at high temperatures. However, we observe none in our measurements here possibly because our experiments were performed in the Ar environment instead of air. Since we are mainly interested in the near-room-temperature behavior of DMMP interacting with  $\text{CeO}_2$  for practical applications, the decomposition products at high temperatures are only briefly mentioned here.

We also monitored the fraction of DMMP that desorbs from  $\text{CeO}_2$ , as is presented in Figure S1. The DMMP signal is integrated on each valley below and above the baseline

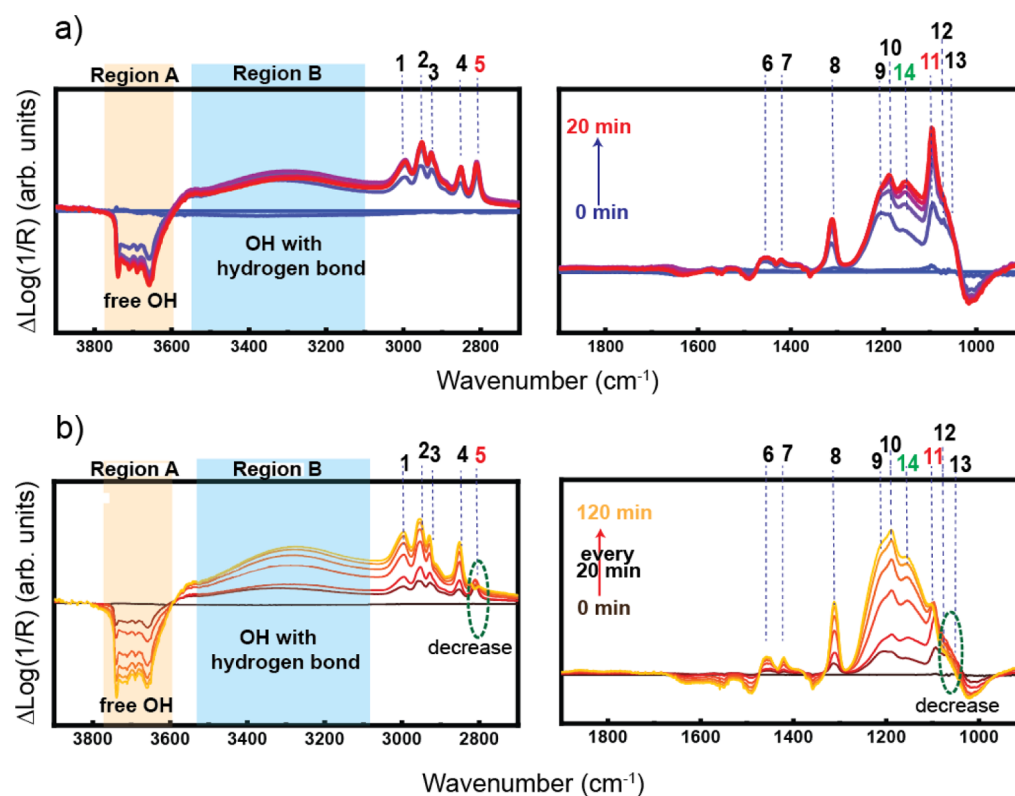


**Figure 5.** (a) *In situ* DRIFTS spectra taken instantly after the first injection of DMMP onto mesoporous CeO<sub>2</sub>. (b) *In situ* DRIFTS spectra taken during the multiple injections of DMMP.

**Table 1.** Assignment of IR Peaks upon DMMP Dosing onto Mesoporous CeO<sub>2</sub> from DRIFTS Characterization

Position	Wavenumber (cm <sup>-1</sup> )	Vibration mode	Assignment
1	3003	$\nu_a$ (PCH <sub>3</sub> )	Intact DMMP
2	2960	$\nu_a$ (OCH <sub>3</sub> )	Intact DMMP
3	2928	$\nu_s$ (PCH <sub>3</sub> )	Intact DMMP
4	2856	$\nu_s$ (PCH <sub>3</sub> )	Intact DMMP
5	2811	$\nu_s$ (MOCH <sub>3</sub> )	methyl from DMMP dissociation
6	1467	$\delta_a$ (OCH <sub>3</sub> ) and $\delta_s$ (OCH <sub>3</sub> )	Intact DMMP
7	1421	$\delta_a$ (PCH <sub>3</sub> )	Intact DMMP
8	1314	$\delta_s$ (PCH <sub>3</sub> )	Intact DMMP
9	1204	$\nu$ (P=O)	Intact DMMP
10	1188	$\rho$ (OCH <sub>3</sub> )	Intact DMMP
11	1096	$\nu$ (OPO)	DMMP dissociation
12	1070	$\nu_a$ (C-O)	methyl as well as DMMP
13	1047	$\nu_s$ (C-O)	methyl as well as DMMP
14	1116-1170	$\nu$ (OPO)	DMMP dissociation

separately to obtain total adsorbed and desorbed DMMP in mesoporous CeO<sub>2</sub> during each heat cycle, as is displayed in Figure S1a. The fraction of desorbed DMMP is plotted in Figure S1b. A lower desorption/adsorption ratio is observed in the first heat cycle, but subsequent cycles give ratios that average about 0.4. Less DMMP desorbing off the surface in the first cycle aligns with the increased product, such as methanol,

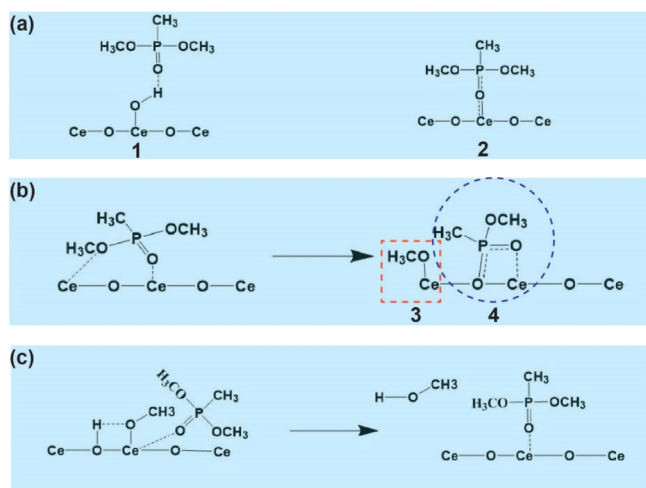
observed in that cycle. After the surface is altered in the first heat cycle, the sorption/desorption ratio remains relatively constant, which is consistent with the observation that methanol production remains similar in subsequent cycles.

**3.3. DMMP Adsorption and Decomposition on Mesoporous CeO<sub>2</sub> at Room Temperature.** Our mass spectrometry measurements indicate that the as-synthesized

mesoporous CeO<sub>2</sub> is active toward DMMP decomposition near room temperature. However, mass spectrometry cannot detect methanol production until MeOH has been desorbed from the CeO<sub>2</sub> surface. Thus, we perform DRIFTS measurement to understand how DMMP would interact with the surface of mesoporous CeO<sub>2</sub> at room temperature. Figure 5a shows the *in situ* DRIFTS spectra taken upon the first injection of DMMP onto mesoporous CeO<sub>2</sub>. The scan right before the first injection is used as a baseline background. The vibration modes corresponding to IR adsorption peaks are assigned based on the literature<sup>11,12,24</sup> and are listed in Table 1. Bands 1–4, 6–10, and 12–13 belong to the different vibration modes of intact DMMP, which was also reported in the study of DMMP on the CeO<sub>2</sub> single crystal surface<sup>24</sup> and other metal oxide systems.<sup>11,22</sup> The spectra between 3100 and 3900 cm<sup>-1</sup> are the characteristic region for the O–H vibration mode. Bands between 3600 and 3800 cm<sup>-1</sup> (region A) are typically associated with “free” OH groups, while modes between 3300 and 3600 cm<sup>-1</sup> (region B) are typically associated with OH groups that are hydrogen-bonded.<sup>11,22</sup>

As is displayed in Figure 5a, upon dosing DMMP, there is a dramatic decrease in the “free” OH groups and an increase in hydrogen-bonded OH groups, which indicates that hydroxylated (–OH-terminated) CeO<sub>2</sub> surfaces interact with DMMP via hydrogen bonds. Previous studies<sup>11,23</sup> propose structure 1 as a major pathway for DMMP to interact with hydroxylated surfaces, as shown in Scheme 2a. Band 5 at 2811 cm<sup>-1</sup> is

**Scheme 2. Proposed configurations after DMMP Interacts with CeO<sub>2</sub> Surfaces:** (a) DMMP Adsorption Configuration on the Surface of CeO<sub>2</sub>; (b) Cleavage of –OCH<sub>3</sub> from DMMP; and (c) Surface Methoxy Group, Replaced by DMMP, Leaving in the Form of Methanol



attributed to the C–H modes of the OCH<sub>3</sub> group when the OCH<sub>3</sub> group directly bonds to a metal center. A clear intensity increase of such a mode indicates the existence of Ce–OCH<sub>3</sub>, resulting from the breaking of the P–OCH<sub>3</sub> bond of DMMP, as shown in structure 3 in Scheme 2b. The strong band 11 at 1096 cm<sup>-1</sup> is due to the ν<sub>s</sub>(O–P–O) vibration when the species has a similar form to structure 4.<sup>11</sup> The observation of clear CeOCH<sub>3</sub> and OPO vibration modes is a strong indication of the dissociation of DMMP on the mesoporous CeO<sub>2</sub> surface at room temperature. Apparently, the dissociation species remains adsorbed to the surface. The broad band(s) 14 observed at 1116–1170 cm<sup>-1</sup> is a mixture of

several bands. Part of this region is reported to belong to ν<sub>a</sub>(O–P–O) as the result of the dissociation of DMMP.<sup>11,12</sup>

Following the first injection of DMMP, multiple injections are also carried out every 20 min. Figure 5b displays the *in situ* DRIFTS spectra taken during the multiple injections of DMMP. Each scan shown in the figure was taken right before the start of each injection. The spectral evolution is very similar to that during the first injection. The continued increase in the intensity of bands 1–4, 6–10, and 12–13 indicates that intact DMMP continues to adsorb on the hydroxylated CeO<sub>2</sub> surface, consuming free surface OH (decrease in region A) and forming hydrogen bonds (increase in region B). This process occurs until the surface reaches saturation. Interestingly, the C–H stretching mode from CeOCH<sub>3</sub> (band 5 at 2811 cm<sup>-1</sup>) increases in intensity during the initial injections, and the intensity decreases in subsequent injections. We attribute the decrease in the CeOCH<sub>3</sub> stretching mode to the decrease in the –OCH<sub>3</sub> group attached to the surface. Band 12 at 1047 cm<sup>-1</sup> and band 13 at 1070 cm<sup>-1</sup> correspond to C–O stretching modes.<sup>22</sup> These two bands also decrease with subsequent injections, further confirming the decrease in the –OCH<sub>3</sub> group attached to the surface. Since we observe the methanol production in our mass spectrometry measurements of DMMP dosing on mesoporous CeO<sub>2</sub>, we conclude that –OCH<sub>3</sub> leaves the CeO<sub>2</sub> surface to form methanol. Also, the replacement of –OCH<sub>3</sub> by DMMP drives the –OCH<sub>3</sub> group leaving the CeO<sub>2</sub> surface. Upon leaving the surface, –OCH<sub>3</sub> groups could take hydrogen from surrounding OH and form methanol as a product. This mechanism, described in a previous study,<sup>11</sup> is illustrated in Scheme 2c. While the CeOCH<sub>3</sub> stretching mode continues to degrade, we observed O–P–O vibration modes (bands 11 and 14) growing, implying that DMMP is still dissociating on the surfaces. Such a phenomenon indicates that DMMP dissociation, which occurs in later injections, does not involve the step whereby OCH<sub>3</sub> binds onto Ce sites (Scheme 2b). Obviously, two different DMMP dissociation pathways happen separately in the DMMP initial and subsequent injections.

**3.4. DFT Modeling of DMMP Adsorption and Decomposition on CeO<sub>2</sub>.** We constructed model CeO<sub>2</sub> surfaces based on our characterization of the mesoporous CeO<sub>2</sub> samples. Our CO adsorption IR characterization indicates that the as-synthesized mesoporous CeO<sub>2</sub> possesses both (110) and (111) surfaces. The XPS spectra and CO adsorption IR measurements show that there exist hydroxylated (OH-terminated) surfaces as well as pristine-like (with exposed undercoordinated Ce atom) surfaces. Thus, we modeled the DMMP interactions with the (110) and (111) CeO<sub>2</sub> surfaces to better understand our experimental observations. For both (110) and (111) surfaces, we also investigated pristine and hydroxylated situations separately to simplify the calculations, although the pristine and hydroxylated surfaces do not exist separately in our mesoporous CeO<sub>2</sub> system.

**3.4.1. DMMP Adsorption on Pristine and Hydroxylated (110) and (111) CeO<sub>2</sub> Surfaces.** Adsorption of DMMP on CeO<sub>2</sub> (110) and (111) surfaces is a straightforward process. Similar to other metal oxides,<sup>17,22,45,55–58</sup> DMMP is adsorbed on the Ce atom via its phosphoryl oxygen, as depicted in Figure 6a,b. The calculated energy of DMMP adsorption on the CeO<sub>2</sub> (110) surface (–164.8 kJ mol<sup>-1</sup>) is considerably higher than that on the (111) surface (–116.9 kJ mol<sup>-1</sup>), which is, most likely, explained by a stronger electrostatic

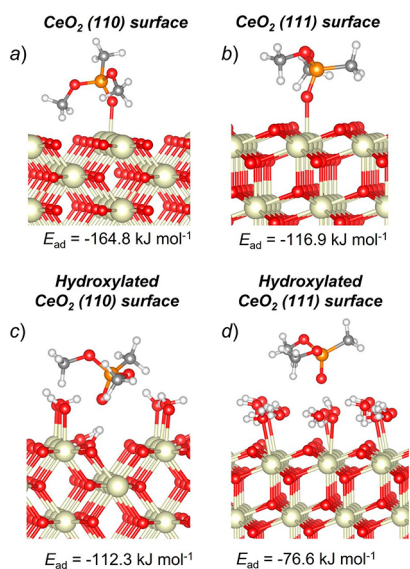


**Figure 6.** Adsorption of DMMP on pristine CeO<sub>2</sub> (a) (110) and (b) (111) surfaces and adsorption of DMMP on hydroxylated CeO<sub>2</sub> (c) (101) and (d) (111) surfaces.

repulsion between the phosphoryl oxygen of DMMP and a surface oxygen atom on the CeO<sub>2</sub> (111) surface. DMMP interacting with the hydroxylated CeO<sub>2</sub> (110) surface forms a hydrogen bond with one of the surface hydroxyls, as shown in Figure 6c. The calculated energy of DMMP adsorption is  $-112.3 \text{ kJ mol}^{-1}$ . Once DMMP is adsorbed on the hydroxylated CeO<sub>2</sub> (111) surface, it interacts with a water molecule via its phosphoryl oxygen, as depicted in Figure 6d. The calculated energy of DMMP adsorption on the CeO<sub>2</sub> (111) surface is  $-76.6 \text{ kJ mol}^{-1}$ .

**3.4.2. DMMP Decomposition on Pristine and Hydroxylated CeO<sub>2</sub> Surfaces.** For DMMP decomposition on CeO<sub>2</sub> (110) and (111) surfaces, we considered two channels associated with the formation of the surface methoxy group. The first channel involves the O–CH<sub>3</sub> bond breaking and the subsequent coordination of the methyl group to the nearest surface oxygen. The second mechanism involves the cleavage of the P–OCH<sub>3</sub> bond. After losing the methoxy group, a new bond is formed between the phosphorus atom and one of the surface oxygen atoms. The methoxy group remains on the surface and forms a bond with a surface Ce atom.

The formation of the methoxy group via the O–CH<sub>3</sub> bond breaking (A1–A2, Figure 7a) on the (110) surface requires  $180.9 \text{ kJ mol}^{-1}$ . The reaction is exothermic with the calculated reaction energy of  $-147.3 \text{ kJ mol}^{-1}$ . A similar mechanism on the CeO<sub>2</sub> (111) surface (B1–B2, Figure 7b) requires  $221.0 \text{ kJ mol}^{-1}$ . The more energetically demanding O–CH<sub>3</sub> bond breaking is less exothermic on the (111) surface ( $-81.7 \text{ kJ mol}^{-1}$ ) than that on the (110) surface ( $-147.3 \text{ kJ mol}^{-1}$ ). The methoxy group formation via the P–OCH<sub>3</sub> bond cleavage on the (110) surface (A1–A3, Figure 7a) requires  $75.7 \text{ kJ mol}^{-1}$ , which is considerably lower than the activation barrier of the process proceeding via the O–CH<sub>3</sub> bond breaking ( $180.9 \text{ kJ mol}^{-1}$ ). The calculated reaction energy of the A1–A3 step is  $-97.5 \text{ kJ mol}^{-1}$ , which reflects a relatively high exothermicity of the reaction. Breaking of the P–OCH<sub>3</sub> bond on the CeO<sub>2</sub> (111) surface (B1–B3–B4) requires a surprisingly low energy of  $24.1 \text{ kJ mol}^{-1}$  (Figure 7b). The reaction proceeds in two steps. The first step (B1–B3) requires  $17.8 \text{ kJ mol}^{-1}$  and

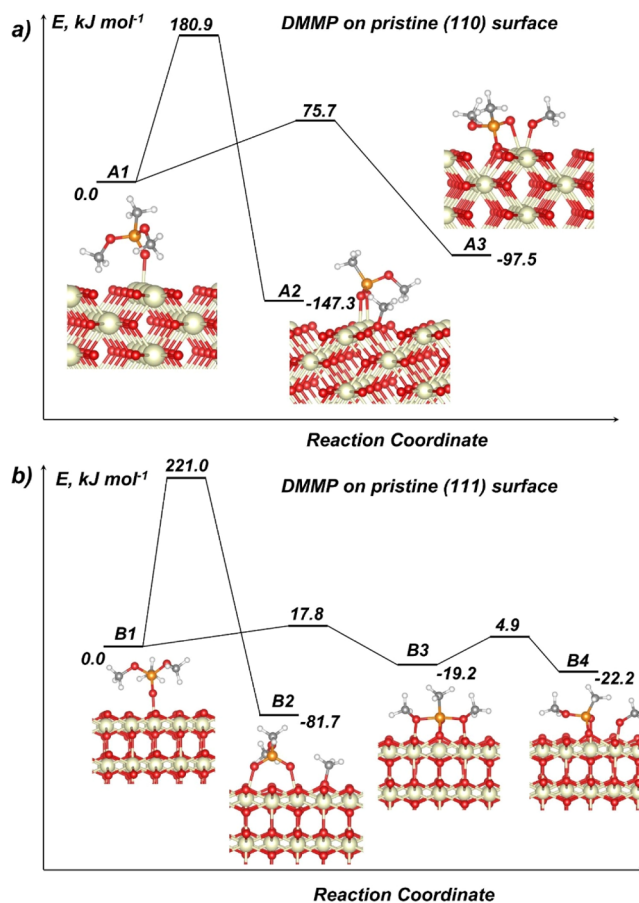


**Figure 7.** Decomposition of DMMP on pristine CeO<sub>2</sub> (a) (110) and (b) (111) surfaces.

involves the formation of a reaction intermediate with 5-coordinated phosphorus atom. Intermediate B3 lies  $19.2 \text{ kJ mol}^{-1}$  lower than the reagent structure. The subsequent decomposition of intermediate B3 via the cleavage of one of the P–OCH<sub>3</sub> bonds requires  $24.1 \text{ kJ mol}^{-1}$ . The overall reaction energy of the mechanism B1–B4 is  $-22.2 \text{ kJ mol}^{-1}$ .

Decomposition of DMMP on the hydroxylated CeO<sub>2</sub> (110) surface yields methanol and can proceed via several plausible channels, which require close activation energies (see the Supporting Information for more details). The most favorable mechanism, that is, the mechanism with the lowest activation energy, is depicted in Figure 8a. The elimination of methanol from the hydroxylated CeO<sub>2</sub> (101) surface proceeds in two steps. The first step (C1–C2) involves the formation of reaction intermediate C2 with a 5-coordinated phosphorus atom. The activation barrier of this step is  $110.2 \text{ kJ mol}^{-1}$ . The intermediate structure C2 corresponds to a shallow minimum on the potential energy surface and lies  $100.9 \text{ kJ mol}^{-1}$  above C1. Breaking of the P–OCH<sub>3</sub> bond in C2 and the subsequent elimination of methanol (C2–C3) require only  $4.6 \text{ kJ mol}^{-1}$ . The overall reaction energy of mechanism C1–C2–C3 is  $-93.5 \text{ kJ mol}^{-1}$ .

Decomposition of DMMP on the hydrated CeO<sub>2</sub> (111) surface also proceeds via the elimination of methanol. Similar to decomposition on hydroxylated CeO<sub>2</sub> (110), the elimination of methanol on CeO<sub>2</sub> (111) proceeds in two steps (Figure 8b). The formation of the reaction intermediate with a coordinated phosphorus atom (D1–D2) on hydroxylated CeO<sub>2</sub> (111) requires  $121.1 \text{ kJ mol}^{-1}$ , which is slightly higher

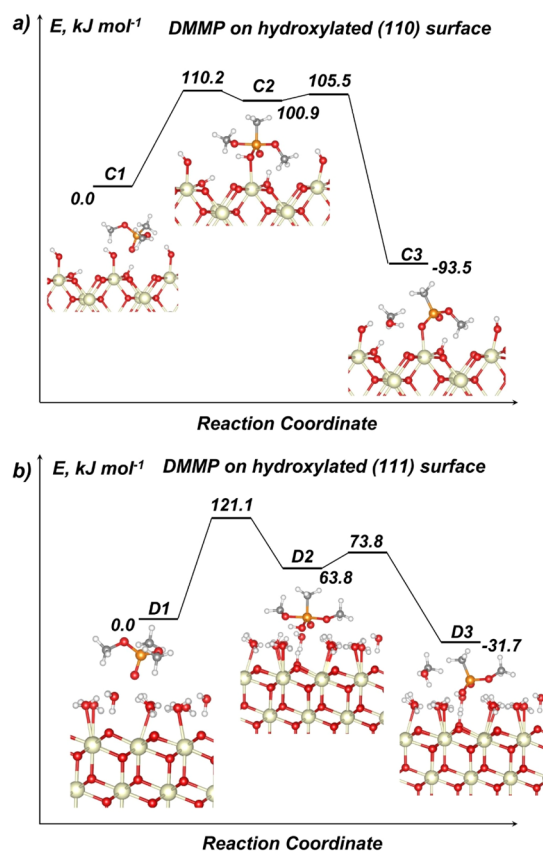


**Figure 8.** Decomposition of DMMP on hydroxylated CeO<sub>2</sub> (a) (110) and (b) (111) surfaces.

than that on the hydroxylated CeO<sub>2</sub> (110) surface (110.2 kJ mol<sup>-1</sup>). Intermediate D2 lies 63.8 kJ mol<sup>-1</sup> higher than D1. The activation barrier of the subsequent methanol elimination from D2 is 10 kJ mol<sup>-1</sup>. The calculated reaction energy of methanol elimination on the CeO<sub>2</sub> (111) surface is -31.7 kJ mol<sup>-1</sup>.

We also modeled a reaction of methanol elimination from DMMP on a hydrated CeO<sub>2</sub> (111) surface proceeding via water molecule displacement (see the [Supporting Information](#) for more details). According to our calculations, this mechanism requires a significantly higher activation energy (207.8 kJ mol<sup>-1</sup>) than the methanol elimination mechanism depicted in [Figure 8](#) and therefore cannot compete with other reactions.

## 4. DISCUSSION

**4.1. DMMP Adsorption through Hydrogen Bonding and Coordinate Covalent Bonding.** Under ambient conditions, the as-synthesized mesoporous CeO<sub>2</sub> has both hydroxylated and pristine-like surfaces, as is implied by the XPS and CO adsorption measurements. Thus, DMMP adsorption occurs on both hydroxylated and pristine-like surfaces of mesoporous CeO<sub>2</sub>. Our calculations of both (110) and (111) surfaces show that the adsorption of DMMP on pristine surfaces is stronger than that on surfaces covered with a monolayer of water as the energy released through DMMP adsorption ( $E_{ad}$ ) on pristine surfaces is significantly larger than that on the hydroxylated surfaces [-164.8 kJ mol<sup>-1</sup> vs -112.3 kJ mol<sup>-1</sup> for the (110) surface and -116.9 kJ mol<sup>-1</sup> vs -76.6 kJ mol<sup>-1</sup> for the (111) surface]. Such a difference in the

adsorption strength on hydroxylated and pristine surfaces originates from the different adsorption mechanisms. As mentioned previously, the DMMP adsorption on the pristine CeO<sub>2</sub> surfaces proceeds through the P=O group coordination to Ce<sup>4+</sup> through oxygen atoms. Ce<sup>4+</sup> has empty f- and d-orbitals. Electron transfer from the P=O group to the empty f- and d-orbitals of Ce<sup>4+</sup> forms a strong covalent coordinative Ce-O=P bond. Alternatively, on the hydroxylated CeO<sub>2</sub> surfaces, DMMP adsorbs through hydrogen bonds of type P=O...H-O. Thus, the adsorption through hydrogen bonding is weaker. These results are consistent with the results of other theoretical studies. For example, we have recently shown that the energy of DMMP adsorption on the pristine ZnO (10 $\bar{1}0$ ) surface is 71 kJ mol<sup>-1</sup> stronger than that on the hydroxylated surface (-142 vs 71 kJ mol<sup>-1</sup>, respectively).<sup>22</sup> Bermudez observed similar trends of DMMP adsorption on pristine and hydroxylated  $\gamma$ -Al<sub>2</sub>O<sub>3</sub> (222 vs 97 kJ mol<sup>-1</sup>, respectively).<sup>56</sup> Typically, the presence of water and hydroxyl groups reduces the energy of DMMP adsorption, making the binding with the surface weaker. The opposite trends were observed for DMMP adsorption on MoO<sub>3</sub>. Our recent study<sup>19</sup> showed that the presence of water is essential for DMMP adsorption on the oxygen-terminated MoO<sub>3</sub> (010) surface.

**4.2. Decomposition of DMMP.** Our DRIFTS measurements during the initial DMMP dosing revealed that the DMMP decomposition involves the formation of surface methoxy groups. With more dosing, DMMP continuously decomposes, while the signal for surface methoxy groups on the surface decreases. In the mass spectroscopy experiments, two methanol production peaks are observed at different temperatures.

Our DFT modeling shows that the formation of surface methoxy groups corresponds to the DMMP decomposition on pristine CeO<sub>2</sub> (110) and (111) surfaces. Decomposition on both hydroxylated (110) and (111) surfaces proceeds via methanol elimination. Although the formation of surface methoxy groups on pristine CeO<sub>2</sub> (110) and (111) surfaces can take place via breaking of either O-CH<sub>3</sub> or P-OCH<sub>3</sub> bonds, as shown in [Figure 7a,b](#), surface-enhanced rupture of the P-OCH<sub>3</sub> bond is the considerably more favorable mechanism on both surfaces. The lower activation energy barrier for P-OCH<sub>3</sub> bond breaking rather than that for PO-CH<sub>3</sub> bond breaking [75.7 vs 180.9 kJ mol<sup>-1</sup> for (110) and 22.7 vs 221 kJ mol<sup>-1</sup> for (111), respectively] can be attributed to the different polarity of the P-O and C-O bonds. The electronegativity values of P, C, and O are 2.2, 2.6, and 3.5, respectively. The difference of the electronegativity between O and P is significantly higher, leading to a larger polarity and a more ionic nature of the P-O bond than that of the C-O bond. Less covalency of the P-O bond makes it easier to break. A recent theoretical study indicates the scission of the P-OR bond as the primary step of the decomposition of phosphate monoesters on the CeO<sub>2</sub> (111) surface with an activation barrier ranging from 12 to 48 kJ/mol.<sup>59</sup> For phosphoric acid, which has a POH group instead of a POR group, the favored dissociation path is through the deprotonation (PO-H breaking) rather than through the P-OH bond cleavage.<sup>60</sup> The different dissociation mechanisms for the POR and POH groups on the CeO<sub>2</sub> surface might originate from the weaker bond strength of PO-H than that of PO-R. The different stabilities of dissociation species (-OR and -R for the POR group and H<sup>+</sup> and -OH for the POH

group) on the surfaces also contribute to the varied dissociation mechanisms.

The cleavage of the P–OCH<sub>3</sub> bond on the CeO<sub>2</sub> (110) surface requires 75.7 kJ mol<sup>-1</sup>, which is significantly lower than activation energies of P–OCH<sub>3</sub> bond cleavage on the ZnO (10 $\bar{1}$ 0) surface (170.6 kJ mol<sup>-1</sup>)<sup>22</sup> and MoO<sub>2</sub> (011) surface (149.2 kJ mol<sup>-1</sup>).<sup>61</sup> Decomposition of DMMP on the CeO<sub>2</sub> (111) surface via P–OCH<sub>3</sub> bond cleavage requires an even lower activation energy (22.7 kJ mol<sup>-1</sup>, Figure 7b). The low activation energy barrier for the cleavage of the P–OCH<sub>3</sub> bond on CeO<sub>2</sub> surfaces explained the observed high activity of mesoporous CeO<sub>2</sub> in the spectroscopic measurements.

The difference in the activation energies of P–OCH<sub>3</sub> bond cleavage on CeO<sub>2</sub> (110) and (111) surfaces is most likely due to different surface structures. Figure 9 shows that in the

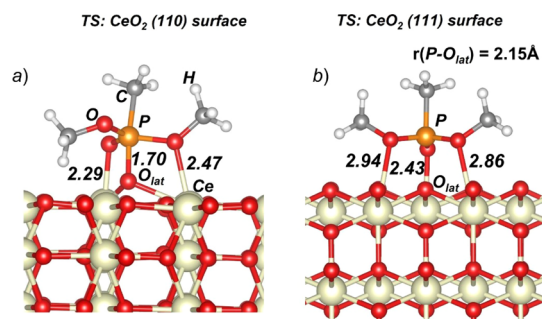


**Figure 9.** Transition-state structures of the P–OCH<sub>3</sub> bond cleavage reaction on CeO<sub>2</sub> (a) (110) and (b) (111) surfaces.

transition-state structure of the P–OCH<sub>3</sub> bond cleavage reaction on the CeO<sub>2</sub> (110) surface, DMMP coordinates to Ce atoms via its phosphoryl oxygen and one of the methoxy oxygens (Figure 9a). In addition, a phosphorus atom is coordinated to lattice oxygen, which leads to the breaking of the bond between the lattice oxygen and cerium atom on the surface. In the transition state localized for P–OCH<sub>3</sub> bond scission on the CeO<sub>2</sub> (111) surface (Figure 9b), DMMP is coordinated to cerium atoms via its phosphoryl and both methoxy oxygen atoms. There is no bond formed between phosphorus and lattice oxygen atoms. As a result, there is no additional perturbation in the system leading to the breaking of bonds between cerium and lattice oxygen atoms.

We found no pathways to form surface methoxy groups upon DMMP decomposition on hydroxylated CeO<sub>2</sub> (110) and hydrated (111) surfaces. In the presence of water and hydroxyl groups, the decomposition of DMMP proceeds via methanol elimination and requires about 110–120 kJ mol<sup>-1</sup> (Figure 8), which is higher than the energy required for DMMP dissociation on the pristine (110) and (111) surfaces.

Based on the comparison of results obtained from DRIFTS, mass spectrometry, and DFT modeling, we conclude that DMMP decomposition on mesoporous CeO<sub>2</sub> proceeds in two steps. The first step corresponds to DMMP decomposition on the dry CeO<sub>2</sub> surface via P–OCH<sub>3</sub> bond cleavage. This mechanism requires a relatively low activation energy of 25–75 kJ mol<sup>-1</sup> (Figure 7). Methoxy groups, which are the main products of DMMP decomposition on pristine surfaces, remain on the surface. This conclusion is consistent with the increased intensity of the corresponding C–H stretching band from M–OCH<sub>3</sub> groups observed in DRIFTS measurements and the absence of the methanol signal in mass spectra at room

temperature. After the areas of the pristine surface are saturated with DMMP and decomposition products, DMMP begins interacting with hydroxylated and hydrated parts of CeO<sub>2</sub> because the elimination of methanol from DMMP in the presence of water requires a noticeably higher energy than the decomposition on the pristine surface (110–120 vs 25–75 kJ mol<sup>-1</sup>, Figures 7 and 8). This second step likely corresponds to the DMMP dissociation observed in the later injections of DMMP from the DRIFTS measurement, where the surface M–OCH<sub>3</sub> group does not form in this dissociation process. A higher activation energy also means that the elimination of methanol is favored at elevated temperatures, which is consistent with mass spectrometry measurements. It is also worth noting that the methanol formation may also be due to the methoxy groups (from DMMP decomposition on pristine CeO<sub>2</sub> surfaces) interacting with the hydroxylated parts of CeO<sub>2</sub> surfaces. Such a process as well as the elimination of methanol from DMMP on the hydroxylated surface might contribute to the two methanol production peaks observed in the mass spectrometry measurements.

## 5. CONCLUSIONS

The as-synthesized high-surface-area mesoporous CeO<sub>2</sub> is proved experimentally to have high reactivity toward DMMP decomposition at room temperature. Our DFT calculations indicate that the activation energy barrier for DMMP dissociation on the pristine (111) surface is the lowest among the metal oxides ever studied.<sup>22,55,57,61</sup> Both the experiments and DFT modeling show the potential of mesoporous CeO<sub>2</sub> to be applied in the protection against CWAs. We note that sarin is different from DMMP in terms of the chemical structure. Thus, investigations on sarin interactions with CeO<sub>2</sub> materials should be performed in the future to get a true understanding and verification on the activity of CeO<sub>2</sub> toward sarin.

As for the materials design perspective, our DFT modeling provides significant insights into the future directions of improving CeO<sub>2</sub> materials for better DMMP adsorption and decomposition. Mesoporous CeO<sub>2</sub> materials should be designed and synthesized to expose more (111) surfaces as this surface displays a lower activation energy barrier for DMMP decomposition. In addition, CeO<sub>2</sub> materials might need to be modified to be less hydrophilic so that there will be more dry pristine surfaces available at ambient conditions, providing stronger DMMP adsorption and higher DMMP decomposition activity on the surface. Such materials design parameters may be achieved through the exploration of different CeO<sub>2</sub> syntheses, postsynthetic modification of the surfaces, or chemical modification of CeO<sub>2</sub> such as isovalent or aliovalent doping.

## ■ ASSOCIATED CONTENT

### Supporting Information

The Supporting Information is available free of charge at <https://pubs.acs.org/doi/10.1021/acsami.1c16668>.

DRIFTS flow line setup for DMMP dosing, temperature-programmed DMMP adsorption and desorption cycles, and detailed discussion on the computational model of water and DMMP interacting with CeO<sub>2</sub> surfaces (PDF)

## AUTHOR INFORMATION

## Corresponding Authors

Maija M. Kuklja – Department of Materials Science and Engineering, University of Maryland, College Park, Maryland 20742, United States; [orcid.org/0000-0002-5047-7734](https://orcid.org/0000-0002-5047-7734); Email: [mkuklja@nsf.gov](mailto:mkuklja@nsf.gov)

Efrain E. Rodriguez – Department of Chemistry and Biochemistry, University of Maryland, College Park, Maryland 20742, United States; [orcid.org/0000-0001-6044-1543](https://orcid.org/0000-0001-6044-1543); Email: [efrain@umd.edu](mailto:efrain@umd.edu)

## Authors

Tianyu Li – Department of Chemistry and Biochemistry, University of Maryland, College Park, Maryland 20742, United States

Roman Tsyshevsky – Department of Materials Science and Engineering, University of Maryland, College Park, Maryland 20742, United States

Lucas Algrim – Department of Chemical and Environmental Engineering, University of California Riverside, Riverside, California 92521, United States

Monica McEntee – US Army Combat Capabilities Development Command Chemical Biological Center, Aberdeen, Maryland 21010, United States

Erin M. Durke – US Army Combat Capabilities Development Command Chemical Biological Center, Aberdeen, Maryland 21010, United States

Bryan Eichhorn – Department of Chemistry and Biochemistry, University of Maryland, College Park, Maryland 20742, United States; [orcid.org/0000-0001-9161-1920](https://orcid.org/0000-0001-9161-1920)

Christopher Karwacki – US Army Combat Capabilities Development Command Chemical Biological Center, Aberdeen, Maryland 21010, United States

Michael R. Zachariah – Department of Chemical and Environmental Engineering, University of California Riverside, Riverside, California 92521, United States; [orcid.org/0000-0002-4115-3324](https://orcid.org/0000-0002-4115-3324)

Complete contact information is available at: <https://pubs.acs.org/10.1021/acsami.1c16668>

## Notes

The authors declare no competing financial interest.

## ACKNOWLEDGMENTS

This work was funded by the Department of Defense (grant HDTRA1-15-1-0005 and HDTRA1-19-1-0001). R.T. and M.M.K. acknowledge support from NSF XSEDE (grant DMR-130077) and DOE NERSC (contract DE-AC02-05CH11231) resources, as well as computational resources at the Maryland Advanced Research Computing Center (MARCC) and University of Maryland supercomputing resources (<http://hpcc.umd.edu>). M.M.K. is grateful to the Office of the Director of National Science Foundation for support under the Independent Research and Development program. Any appearance of findings, conclusions, or recommendations expressed in this material are those of the authors and do not necessarily reflect the views of NSF.

## REFERENCES

(1) Ebrahim, A. M.; Plonka, A. M.; Tian, Y.; Senanayake, S. D.; Gordon, W. O.; Balboa, A.; Wang, H.; Collins-Wildman, D. L.; Hill, C. L.; Musaev, D. G.; Morris, J. R.; Troya, D.; Frenkel, A. I.

Multimodal Characterization of Materials and Decontamination Processes for Chemical Warfare Protection. *ACS Appl. Mater. Interfaces* **2019**, *12*, 14721–14738.

(2) Gibbons, W. T.; Holdren, S.; Hu, J.; Eichhorn, B. W.; Zachariah, M. R. Fixed Feed Temperature-Programmed Modulation - A Quantitative Method to Obtain Thermophysical Parameters: Application to Chemical Warfare Agent Adsorbents. *J. Phys. Chem. C* **2019**, *123*, 12694–12705.

(3) Morrison, R. W. *NBC Filter Performance*; Edgewood Chemical Biological Center, 2001.

(4) Ekerdt, J. G.; Klabunde, K. J.; Shapley, J. R.; White, J. M.; Yates, J. T. Surface Chemistry of Organophosphorus Compounds. *J. Phys. Chem.* **1988**, *92*, 6182–6188.

(5) Aurian-Blajeni, B.; Boucher, M. M. Interaction of Dimethyl Methylphosphonate with Metal Oxides. *Langmuir* **1989**, *5*, 170–174.

(6) Mukhopadhyay, S.; Schoenitz, M.; Dreizin, E. L. Vapor-Phase Decomposition of Dimethyl Methylphosphonate (DMMP), a Sarin Surrogate, in Presence of Metal Oxides. *Def. Technol.* **2021**, *17*, 1095–1114.

(7) Novak, T. G.; DeSario, P. A.; Long, J. W.; Rolison, D. R. Designing Oxide Aerogels With Enhanced Sorptive and Degradative Activity for Acute Chemical Threats. *Front. Mater.* **2021**, *8*, 67479.

(8) Gu, D.; Schüth, F. Synthesis of Non-Siliceous Mesoporous Oxides. *Chem. Soc. Rev.* **2014**, *43*, 313–344.

(9) Ren, Y.; Ma, Z.; Bruce, P. G. Ordered Mesoporous Metal Oxides: Synthesis and Applications. *Chem. Soc. Rev.* **2012**, *41*, 4909–4927.

(10) Rusu, C. N.; Yates, J. T. J. Adsorption and Decomposition of Dimethyl Methylphosphonate on TiO<sub>2</sub>. *J. Phys. Chem. B* **2000**, *104*, 12292–12298.

(11) Panayotov, D. A.; Morris, J. R. J. Uptake of a Chemical Warfare Agent Simulant (DMMP) on TiO<sub>2</sub>: Reactive Adsorption and Active Site Poisoning. *Langmuir* **2009**, *25*, 3652–3658.

(12) Panayotov, D. A.; Morris, J. R. Thermal Decomposition of a Chemical Warfare Agent Simulant (DMMP) on TiO<sub>2</sub>: Adsorbate Reactions with Lattice Oxygen as Studied by Infrared Spectroscopy. *J. Phys. Chem. C* **2009**, *113*, 15684–15691.

(13) Tsyshevsky, R.; McEntee, M.; Durke, E. M.; Karwacki, C.; Kuklja, M. M. Degradation of Fatal Toxic Nerve Agents on Dry TiO<sub>2</sub>. *ACS Appl. Mater. Interfaces* **2021**, *13*, 696–705.

(14) Jeon, S.; Schweigert, I. V.; Pehrsson, P. E.; Balow, R. B. Kinetics of Dimethyl Methylphosphonate Adsorption and Decomposition on Zirconium Hydroxide Using Variable Temperature in Situ Attenuated Total Reflection Infrared Spectroscopy. *ACS Appl. Mater. Interfaces* **2020**, *12*, 14662–14671.

(15) Balow, R. B.; Lundin, J. G.; Daniels, G. C.; Gordon, W. O.; McEntee, M.; Peterson, G. W.; Wynne, J. H.; Pehrsson, P. E. Environmental Effects on Zirconium Hydroxide Nanoparticles and Chemical Warfare Agent Decomposition: Implications of Atmospheric Water and Carbon Dioxide. *ACS Appl. Mater. Interfaces* **2017**, *9*, 39747–39757.

(16) Templeton, M. K.; Weinberg, W. H. Adsorption and Decomposition of Dimethyl Methylphosphonate on an Aluminum Oxide Surface. *J. Am. Chem. Soc.* **2002**, *124*, 97–108.

(17) Trotochaud, L.; Tsyshevsky, R.; Holdren, S.; Fears, K.; Head, A. R.; Yu, Y.; Karşlıoğlu, O.; Pletincx, S.; Eichhorn, B.; Owrutsky, J.; Long, J.; Zachariah, M.; Kuklja, M. M.; Bluhm, H. Spectroscopic and Computational Investigation of Room-Temperature Decomposition of a Chemical Warfare Agent Simulant on Polycrystalline Cupric Oxide. *Chem. Mater.* **2017**, *29*, 7483–7496.

(18) Yoo, R.; Yoo, S.; Lee, D.; Kim, J.; Cho, S.; Lee, W. Highly Selective Detection of Dimethyl Methylphosphonate (DMMP) Using CuO Nanoparticles /ZnO Flowers Heterojunction. *Sens. Actuators, B* **2017**, *240*, 1099–1105.

(19) Head, A. R.; Tsyshevsky, R.; Trotochaud, L.; Yu, Y.; Kyhl, L.; Karşlıoğlu, O.; Kuklja, M. M.; Bluhm, H. Adsorption of Dimethyl Methylphosphonate on MoO<sub>3</sub>: The Role of Oxygen Vacancies. *J. Phys. Chem. C* **2016**, *120*, 29077–29088.

- (20) Head, A. R.; Tang, X.; Hicks, Z.; Wang, L.; Bleuel, H.; Holdren, S.; Trotochaud, L.; Yu, Y.; Kyhl, L.; Karlıoğlu, O.; Fears, K.; Owrutsky, J.; Zachariah, M.; Bowen, K. H.; Bluhm, H. Thermal Desorption of Dimethyl Methylphosphonate from MoO<sub>3</sub>. *Catal. Struct. React.* **2017**, *3*, 112.
- (21) Tesfai, T. M.; Sheinker, V. N.; Mitchell, M. B. Decomposition of Dimethyl Methylphosphonate (DMMP) on Alumina-Supported Iron Oxide. *J. Phys. Chem. B* **1998**, *102*, 7299–7302.
- (22) Holdren, S.; Tsyshkevsky, R.; Fears, K.; Owrutsky, J.; Wu, T.; Wang, X.; Eichhorn, B. W.; Zachariah, M. R.; Zachariah, R. Adsorption and Destruction of the G-Series Nerve Agent Simulant Dimethyl Methylphosphonate on Zinc Oxide. *ACS Catal.* **2018**, *9*, 902–911.
- (23) Gordon, W. O.; Tissue, B. M.; Morris, J. R. Adsorption and Decomposition of Dimethyl Methylphosphonate on Y<sub>2</sub>O<sub>3</sub> Nanoparticles. *J. Phys. Chem. C* **2007**, *111*, 3233–3240.
- (24) Chen, D. A.; Ratliff, J. S.; Hu, X.; Gordon, W. O.; Senanayake, S. D.; Mullins, D. R. Dimethyl Methylphosphonate Decomposition on Fully Oxidized and Partially Reduced Ceria Thin Films. *Surf. Sci.* **2010**, *604*, 574–587.
- (25) Ma, R.; Zhang, S.; Wen, T.; Gu, P.; Li, L.; Zhao, G.; Niu, F.; Huang, Q.; Tang, Z.; Wang, X. A Critical Review on Visible-Light-Response CeO<sub>2</sub>-Based Photocatalysts with Enhanced Photooxidation of Organic Pollutants. *Catal. Today* **2019**, *335*, 20–30.
- (26) Trovarelli, A. Catalytic Properties of Ceria and CeO<sub>2</sub>-Containing Materials. *Catal. Rev.—Sci. Eng.* **1996**, *38*, 439–520.
- (27) Montini, T.; Melchionna, M.; Monai, M.; Fornasiero, P. Fundamentals and Catalytic Applications of CeO<sub>2</sub>-Based Materials. *Chem. Rev.* **2016**, *116*, 5987–6041 American Chemical Society May.
- (28) Trenque, I.; Magnano, G. C.; Bolzinger, M. A.; Roiban, L.; Chaput, F.; Pitault, I.; Briançon, S.; Devers, T.; Masenelli-Varlot, K.; Bugnet, M.; Amans, D. Shape-Selective Synthesis of Nanoceria for Degradation of Paraoxon as a Chemical Warfare Simulant. *Phys. Chem. Chem. Phys.* **2019**, *21*, 5455–5465.
- (29) Salerno, A.; Pitault, I.; Devers, T.; Pelletier, J.; Briançon, S. Model-Based Optimization of Parameters for Degradation Reaction of an Organophosphorus Pesticide, Paraoxon, Using CeO<sub>2</sub> Nanoparticles in Water Media. *Environ. Toxicol. Pharmacol.* **2017**, *53*, 18–28.
- (30) Henych, J.; Janoš, P.; Kormunda, M.; Tolasz, J.; Štengl, V. Reactive Adsorption of Toxic Organophosphates Parathion Methyl and DMMP on Nanostructured Ti/Ce Oxides and Their Composites. *Arabian J. Chem.* **2019**, *12*, 4258–4269.
- (31) Mitchell, M. B.; Tesfamichael, A. B.; Nunley, M.; Gatimu, N.; Nunley, M. Decomposition of Dimethyl Methylphosphonate (DMMP) on Supported Cerium and Iron Co-Impregnated Oxides at Room Temperature. *J. Phys. Chem. B* **2002**, *107*, 580–586.
- (32) Laha, S. C.; Ryoo, R. Synthesis of Thermally Stable Mesoporous Cerium Oxide with Nanocrystalline Frameworks Using Mesoporous Silica Templates. *Chem. Commun.* **2003**, *3*, 2138–2139.
- (33) Ji, P.; Zhang, J.; Chen, F.; Anpo, M. Ordered Mesoporous CeO<sub>2</sub> Synthesized by Nanocasting from Cubic Ia3d Mesoporous MCM-48 Silica: Formation, Characterization and Photocatalytic Activity. *J. Phys. Chem. C* **2008**, *112*, 17809–17813.
- (34) Kim, T.-W.; Kleitz, F.; Paul, B.; Ryoo, R. MCM-48-like Large Mesoporous Silicas with Tailored Pore Structure: Facile Synthesis Domain in a Ternary Triblock Copolymer–Butanol–Water System. *J. Am. Chem. Soc.* **2005**, *127*, 7601–7610.
- (35) Cheary, R. W.; Coelho, A. Fundamental Parameters Approach to X-Ray Line-Profile Fitting. *J. Appl. Crystallogr.* **1992**, *25*, 109–121.
- (36) Harvey, J. A.; McEntee, M. L.; Garibay, S. J.; Durke, E. M.; DeCoste, J. B.; Greathouse, J. A.; Sava Gallis, D. F. Spectroscopically Resolved Binding Sites for the Adsorption of Sarin Gas in a Metal–Organic Framework: Insights beyond Lewis Acidity. *J. Phys. Chem. Lett.* **2019**, *10*, 5142–5147.
- (37) Kohn, W.; Sham, L. J. Self-Consistent Equations Including Exchange and Correlation Effects. *Phys. Rev.* **1965**, *140*, A1133–A1138.
- (38) Hohenberg, P.; Kohn, W. Inhomogeneous Electron Gas. *Phys. Rev.* **1964**, *136*, B864–B871.
- (39) Perdew, J. P.; Burke, K.; Ernzerhof, M. Generalized Gradient Approximation Made Simple. *Phys. Rev. Lett.* **1996**, *77*, 3865–3868.
- (40) Blöchl, P. E. Projector Augmented-Wave Method. *Phys. Rev. B: Condens. Matter Mater. Phys.* **1994**, *50*, 17953–17979.
- (41) Kresse, G.; Hafner, J. Ab Initio Molecular Dynamics for Liquid Metals. *Phys. Rev. B: Condens. Matter Mater. Phys.* **1993**, *47*, 558–561.
- (42) Kresse, G.; Furthmüller, J. Efficient Iterative Schemes for Ab Initio Total-Energy Calculations Using a Plane-Wave Basis Set. *Phys. Rev. B: Condens. Matter Mater. Phys.* **1996**, *54*, 11169–11186.
- (43) Kresse, G.; Furthmüller, J. Efficiency of Ab-Initio Total Energy Calculations for Metals and Semiconductors Using a Plane-Wave Basis Set. *Comput. Mater. Sci.* **1996**, *6*, 15–50.
- (44) Dudarev, S. L.; Botton, G. A.; Savrasov, S. Y.; Humphreys, C. J.; Sutton, A. P. Electron-Energy-Loss Spectra and the Structural Stability of Nickel Oxide: An LSDA+U Study. *Phys. Rev. B: Condens. Matter Mater. Phys.* **1998**, *57*, 1505–1509.
- (45) Tosoni, S.; Pacchioni, G. Trends in Adhesion Energies of Gold on MgO(100), Rutile TiO<sub>2</sub>(110), and CeO<sub>2</sub>(111) Surfaces: A Comparative DFT Study. *J. Phys. Chem. C* **2017**, *121*, 28328–28338.
- (46) Grimme, S. Semiempirical GGA-Type Density Functional Constructed with a Long-Range Dispersion Correction. *J. Comput. Chem.* **2006**, *27*, 1787–1799.
- (47) Henkelman, G.; Uberuaga, B. P.; Jónsson, H. Climbing Image Nudged Elastic Band Method for Finding Saddle Points and Minimum Energy Paths. *J. Chem. Phys.* **2000**, *113*, 9901–9904.
- (48) Adu, K. W.; Xiong, Q.; Gutierrez, H. R.; Chen, G.; Eklund, P. C. Raman Scattering as a Probe of Phonon Confinement and Surface Optical Modes in Semiconducting Nanowires. *Appl. Phys. A: Mater. Sci. Process.* **2006**, *85*, 287–297.
- (49) Faraci, G.; Gibilisco, S.; Pennisi, A. R.; Faraci, C. Quantum Size Effects in Raman Spectra of Si Nanocrystals. *J. Appl. Phys.* **2011**, *109*(), 074311. <https://doi.org/10.1063/1.3567908>. DOI: 10.1063/1.3567908
- (50) Paparazzo, E. Use and Mis-Use of x-Ray Photoemission Spectroscopy Ce<sub>3d</sub> Spectra of Ce<sub>2</sub>O<sub>3</sub> and CeO<sub>2</sub>. *J. Phys. Condens. Matter* **2018**, *30*, 343003.
- (51) Yang, C.; Yu, X.; Heißler, S.; Nefedov, A.; Colussi, S.; Llorca, J.; Trovarelli, A.; Wang, Y.; Wöll, C. Surface Faceting and Reconstruction of Ceria Nanoparticles. *Angew. Chem., Int. Ed.* **2017**, *56*, 375–379.
- (52) Wang, Y.; Wöll, C. IR Spectroscopic Investigations of Chemical and Photochemical Reactions on Metal Oxides: Bridging the Materials Gap. *Chem. Soc. Rev.* **2017**, *46*, 1875–1932.
- (53) Mullins, D. R. The Surface Chemistry of Cerium Oxide. *Surf. Sci. Rep.* **2015**, *70*, 42–85.
- (54) Segal, S. R.; Cao, L.; Suib, S. L.; Tang, X.; Satyapal, S. Thermal Decomposition of Dimethyl Methylphosphonate over Manganese Oxide Catalysts. *J. Catal.* **2001**, *198*, 66–76.
- (55) Bermudez, V. M. Quantum-Chemical Study of the Adsorption of DMMP and Sarin on  $\gamma$ -Al<sub>2</sub>O<sub>3</sub>. *J. Phys. Chem. C* **2007**, *111*, 3719–3728.
- (56) Bermudez, V. M. Computational Study of Environmental Effects in the Adsorption of DMMP, Sarin, and VX on  $\gamma$ -Al<sub>2</sub>O<sub>3</sub>: Photolysis and Surface Hydroxylation. *J. Phys. Chem. C* **2009**, *113*, 1917–1930.
- (57) Quintero, Y. C.; Nagarajan, R. Molecular and Dissociative Adsorption of DMMP, Sarin and Soman on Dry and Wet TiO<sub>2</sub>(110) Using Density Functional Theory. *Surf. Sci.* **2018**, *675*, 26–35.
- (58) Walenta, C. A.; Xu, F.; Tesvara, C.; O'Connor, C. R.; Sautet, P.; Friend, C. M. Facile Decomposition of Organophosphonates by Dual Lewis Sites on a Fe<sub>3</sub>O<sub>4</sub>(111) Film. *J. Phys. Chem. C* **2020**, *124*, 12432–12441.
- (59) Zhao, C.; Xu, Y. Theoretical Investigation of Dephosphorylation of Phosphate Monoesters on CeO<sub>2</sub>(111). *Catal. Today* **2018**, *312*, 141–148.

(60) Bhasker-Ranganath, S.; Zhao, C.; Xu, Y. Theoretical Analysis of the Adsorption of Phosphoric Acid and Model Phosphate Monoesters on CeO<sub>2</sub>(111). *Surf. Sci.* **2021**, *705*, 121776.

(61) Head, A. R.; Tsyshevsky, R.; Trotochaud, L.; Yu, Y.; Karşlıoğlu, O.; Eichhorn, B.; Kuklja, M. M.; Bluhm, H. Dimethyl Methylphosphonate Adsorption and Decomposition on MoO<sub>2</sub> as Studied by Ambient Pressure X-Ray Photoelectron Spectroscopy and DFT Calculations. *J. Phys. Condens. Matter* **2018**, *30*, 134005.